

# Kinetics of the major coal seam in typical coal mining areas of Southern Junggar coalfield, Xinjiang, China

Li Shen

Xinjiang University

Qiang Zeng (✉ [zengqiang@xju.edu.cn](mailto:zengqiang@xju.edu.cn))

Xinjiang University

---

## Research

**Keywords:** Southern Junggar coalfield, functional group, oxygen consumption rate, activation 33 energy, exothermic heat

**Posted Date:** April 24th, 2020

**DOI:** <https://doi.org/10.21203/rs.3.rs-23673/v1>

**License:**   This work is licensed under a Creative Commons Attribution 4.0 International License.

[Read Full License](#)

---

# Kinetics of the major coal seam in typical coal mining areas of Southern Junggar coalfield, Xinjiang, China

SHEN Li<sup>1, 2, 3</sup>, ZENG Qiang<sup>1, 2, 3\*</sup>

1. School of Resource and Environment Sciences, Xinjiang University, Urumqi 830046, China;

2. Institute for Ecology and Environment, Xinjiang University, Urumqi 830046, China;

3. Key Laboratory of Oasis of Ministry of Education, Xinjiang University, Urumqi 830046, China

\*Corresponding author: Qiang Zeng

Email: [zengqiang@xju.edu.cn](mailto:zengqiang@xju.edu.cn)

Tel./Fax: +86 991 8552056

**Abstract:** In the present study, the authors collected coal samples from the Wudong (WD), Dahuangshan (DHS), and Sikeshu (SKS) coal mines in the Southern Junggar coalfield. The collected coal was ground into particle sizes of 0.25–0.38 mm, 0.15–0.18 mm, 0.109–0.12 mm, 0.08–0.096 mm, and <0.075 mm. The experimental data was acquired using diverse methods, such as in situ infrared spectroscopic analysis, temperature-programmed oxidation, and thermogravimetric analysis. The results show that the number of oxygen-containing functional groups increased with the decline in particle size, indicating that a smaller particle size may facilitate oxidation reactions and spontaneous coal combustion. On the basis of the analysis of the elements of coal samples, it can be concluded that the proportion of oxygen elements of coal samples in three mining areas is:  $WD > SKS > SHS$ . The oxygen consumption rate of the DHS and WD coal samples increased exponentially when the temperature increased; the rate of SKS coal samples initially rose significantly and then decreased. The gas generation rates for the different gases indicated that temperatures of 90 °C or 130 °C could accelerate the oxidation reaction. The pollutants produced by the oxidation of the SKS coal samples were higher than those by DHS and WD. For all particle diameters, the  $T_3$  for the SKS samples is smaller than that for WD and DHS, indicating that the SKS coal sample will combust more readily. With the decrease in particle size, the activation energy showed an increase in low-temperature oxidation stage. While the activation energy of the WD and SKS samples decreased in high temperature stage, that of the DHS increased before decreasing. A lower of activation energy means that the coal will have a higher risk of spontaneous combustion. Based on the differential scanning calorimetry (DSC) curve, SKS coal sample has the highest exothermic heat, the DHS has the second, and WD has the least. With

31 a higher exothermic heat, the coal sample will more readily ignite.

32 **Keywords:** Southern Junggar coalfield, functional group, oxygen consumption rate, activation  
33 energy, exothermic heat

## 34 1. Introduction

35 Coal is prone to spontaneous combustion in underground mining (Cheng et al., 2017). Coal  
36 oxidation at low temperatures is the heat source liable for the self-heating and spontaneous  
37 combustion of coal. Self-heating of coal begins when adequate oxygen from the air is sufficient to  
38 support the reaction between coal and oxygen. The heat produced by low-temperature oxidation of  
39 coal is not sufficiently dissipated either by conduction or convection, hence an increase in  
40 temperature within the coal mass arises (Onifade et al., 2020, 2019). Coal spontaneous combustion  
41 (CSC) causes huge economic losses and casualties, with the toxic and harmful gases produced  
42 during coal combustion not only polluting the working environment, but also causing great  
43 damage to the ecological environment (Kong et al., 2017). Some scholars (Niu et al., 2017; Peña et  
44 al., 2018; Wang et al., 2018; Liu et al., 2018) have studied various aspects of coal (e.g. geological  
45 conditions, moisture content, and particle size) to prevent fires from CSC and control the pollution  
46 from the burning coal.

47 Oxidative combustion of coal is a complex physico-chemical process affected by many  
48 internal and external factors such as the degree of metamorphism, coal rock composition, coal  
49 molecular structure, moisture, volatile matter, ash, carbon, hydrogen, nitrogen and total sulfur  
50 contents, particle size, temperature, heating rate, air leakage intensity (Zhang et al., 2020; Kong et  
51 al., 2018; Zhang, 2004). (Zhao et al., 2019 (a)) conducted X-ray diffraction (XRD) and  
52 Fourier-transform infrared spectroscopy (FTIR) analyses on three fresh bituminous coal samples  
53 from the Huainan Coal Mine of China to determine the microscopic characteristics of coal during  
54 high-temperature oxidation. Through FTIR, Raman spectroscopy, and solid-state <sup>13</sup>C NMR  
55 spectroscopy, (Mustafa Baysal et al., 2016) studied the chemical composition and degree of  
56 ordered structure in Turkish lignite. (QU et al., 2018) experimentally analysed the correlation of  
57 coal with varying metamorphic grades as well as the influencing factors of characteristic  
58 temperature. Using the ultrasonic extraction and FTIR approaches, (Zhang et al., 2019) and (Xu et  
59 al., 2018) investigated the rate of change of the primary oxygen-containing functional groups  
60 during the low-temperature oxidation of coal and the chemical reactions of free radicals with  
61 functional groups during the spontaneous combustion of coal. (Wang et al., 2018) examined the

62 relationship between free radicals, apparent activation energy, and functional groups in the  
63 low-temperature oxidation process of Jurassic coal in northern Shaanxi. Using the FTIR approach,  
64 (Yan et al., 2018) quantitatively analysed the characteristics of surface functional groups of coal  
65 coke in an O<sub>2</sub> or CO<sub>2</sub> atmosphere. (Pan et al., 2020) used XRD and FTIR to comparatively analyse  
66 the rate of change in the coal oxidation microstructures under varying temperatures and oxygen  
67 conditions. (Xiao et al., 2018) used a 15-ton experimental furnace and a simultaneous thermal  
68 analyser to investigate the full process of the first and second stages of spontaneous combustion by  
69 analysing the change in temperature, mass, thermal energy intensity, and gaseous products through  
70 FTIR.

71 The oxidative combustion process of coal need to be researched further, used a  
72 temperature-programmed test device for spontaneous combustion, (Deng et al., 2019) studied the  
73 effect of particle size on the activation energy of the oxidation reaction of the coal. (Zeng et al.,  
74 2017) used a temperature-programmed oxidation test device to conducting an oxidation property  
75 experiment on a significant coal seam (Bm) in the Dajing mining area of the Eastern Junggar  
76 Coalfield. They investigated many aspects of spontaneous combustion of coal samples with  
77 different particle sizes, including the critical temperature (T<sub>c</sub>), initial temperature of CO, Graham's  
78 ratio, temperature-dependent CO and O<sub>2</sub> concentrations, and initial temperature of other C<sub>n</sub>H<sub>m</sub>  
79 gases. (Yang et al., 2018) investigated the relationship between spontaneous combustion and  
80 indicator gases to seek an effective solution for the spontaneous combustion of the No. 72 coal  
81 seam of the Erjing coal mine in Yuandian.

82 The dynamic characteristics of coal play an important role in oxidative combustion. (Zhao et  
83 al., 2019 (b))Using the thermogravimetric analysis plus the differential scanning calorimetry  
84 (TGA-DSC) approach, they divided the high-temperature oxidation process into four sub-stages  
85 and identified detailed characteristics of exothermic heat. Using a self-made programmed  
86 experimental system, they maintained the temperature parameters at a specified level to simulate  
87 the combustion characteristics of coal. Using the TGA approach and FactSage software, (Zhu et al.,  
88 2019) studied the release of minerals and thermal change and transition behaviours in mixed ashes.  
89 They also analysed the morphological and chemical characteristics of ash deposition on the  
90 heating surface of the boiler in which the two types of coal were burned. (Casal et al., 2018)  
91 investigated the pyrolysis characteristics of a series of bituminous coal, anthracite, and lignite  
92 using TGA. (Lei et al.,2018) built a large 2-ton experimental furnace and used coal samples from

93 Dafosi to conduct an oxidation experiment, simulating the spontaneous combustion of coal at a  
94 low temperature (<100°C). These studies can be applied to provide a theoretical basis for CSC.  
95 Despite the comprehensive researches concentrated on the effects of internal and external  
96 factors (e.g. coal analysis, microstructure, indicator gases, and kinetic parameters of coal samples),  
97 there are few studies on the aspects of coal during the low-temperature oxidation and heating  
98 process. However, related studies of spontaneous combustion in the major coal seams of the  
99 Xinjiang's Southern Junggar coalfield need to be explored further.

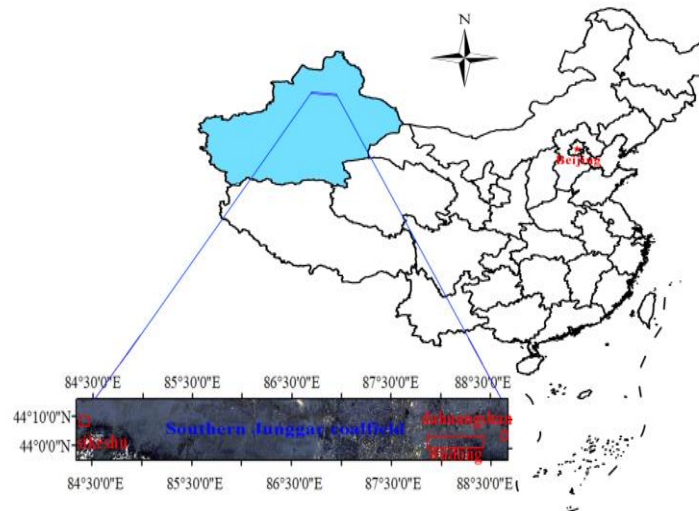
100 Considering the severity of CSC in Xinjiang and the weakness in the related fundamental  
101 studies, combustible coal samples from three mining areas of the same coalfield were acquired to  
102 test the variation in the molecular functional groups of coal with different particle sizes through  
103 FTIR. A temperature-programmed experiment was conducted to investigate the quantity of  
104 gaseous products and amount of oxygen consumption in low-temperature oxidation processes.  
105 Using the TGA, this study analysed the characteristic temperature, activation energy, and  
106 exothermic heat of three types of coal samples with different particle sizes to determine the  
107 spontaneous combustibility of coal. This study used FTIR technology to further evaluate the  
108 chemical significance of the coal molecule parameters and explain the differences in the structural  
109 changes. Moreover, the molecular parameters were linked with the thermo-kinetics of  
110 low-temperature coal oxidation to construct the fundamental theory of spontaneous combustion in  
111 the studied mines. Finally, this study investigated the micro-chemical structure and  
112 low-temperature and high-temperature oxidation characteristics of coal from the Southern Junggar  
113 coalfield. The intent is to uncover the macro and micro changes and kinetic characteristics of  
114 coal-oxygen reactions, thus providing a theoretical foundation for fire prevention and control in  
115 coalfields.

## 116 **2. Materials and Methodology**

117 The Southern Junggar coalfield (Fig. 1), which is the primary coal-bearing region of Xinjiang,  
118 is located along the northern foothills of the Tianshan Mountains and the southern margin of the  
119 Junggar Basin. Along the west, it stretches from west of the Sikeshe Coal Mine (SKS) in Wusu  
120 County to the east of Shuixigou in Jimusaer County. The coalfield is approximately 450 km long  
121 from east to west, presenting a zonal distribution in the east-west direction. The coalfield is  
122 conveniently located, with roads extending in various directions.

123 The Sikeshe coal mine (SKS) is located along the northern foothills of the Tianshan

124 Mountain and the southern margin of the Junggar Basin, approximately 40 km southwest of Wusu  
 125 City. It is part of the Southern Junggar coalfield and is the main coal producer in the  
 126 Wusu-Kuytun-Dushanzi golden region. The Wudong Coal Mine (WD) is located near the southern  
 127 margin of the Junggar Basin and in the middle of the Southern Junggar coalfield. The thickness of  
 128 its coal seam varies significantly, tending to be thick in the east and thin toward the west, and the  
 129 seams are steeply inclined. The horizontal stratification and fully mechanised top coal caving  
 130 methods have been adopted for mining WD. Presently, the primary coal seam is Group B, and the  
 131 coal type is dominated by weak caking coal. The Dahuangshan Coal Mine (DHS) is 120 km east  
 132 of Urumqi City and 60 km from Fukang City. It is controlled by Fukang City, Changji Hui  
 133 Autonomous Prefecture. The coal seam of the DHS is extremely thick and tilted at an angle.



134

Fig. 1. Location of study area

135

### 136 2.1 Preparation of coal samples and analysis of coal property

137 The coal samples used in this study were collected from the WD, DHS, and SKS mines in the  
 138 Southern Junggar coalfield. The collected raw coal was crushed and screened to produce samples  
 139 with various particle sizes: 0.25 to 0.38 mm, 0.15 to 0.18 mm, 0.109 to 0.12 mm, 0.08 to 0.096  
 140 mm, and <0.075 mm. Table 1 presents an analysis of the properties of the collected coal samples.

141 Table 1

### 142 Proximate and elemental analysis of coal samples

Sample	Proximate analysis/wt%, ad				Elemental analysis/wt%,daf				S/wt%	Water/wt%
	$M_{ad}$	$A_d$	$V_{da}$	$FC_{ad}$	$C_d$	$H_d$	$O_d$	$N_d$	$S_{t,d}$	$M_t$
WD	1.91	4.32	32.26	64.81	71.88	4.67	18.01	0.85	0.27	2.50

DHS	1.74	10.48	43.47	50.60	72.78	4.91	10.53	1.06	0.24	2.6
SKS	6.52	7.73	51.39	44.85	69.29	5.45	16.61	0.75	0.17	11.7

144 2.2 Methodology

145 2.2.1 Infrared Spectroscopy Analysis

146 A VERTEX 70 FTIR device (made by Germany's Bruker) was used. Experimental conditions  
 147 were as follows: RES 4.0  $\text{cm}^{-1}$ , SCANS 120, and wavelength in the range of 400 to 4,000  $\text{cm}^{-1}$ .

148 2.2.2 Temperature-Programmed Oxidation (TPO) Analysis

149 The intact coal samples were crushed, and five coal samples with particle sizes of 0.25–0.38  
 150 mm, 0.15–0.18 mm, 0.109–0.12 mm, 0.08–0.096 mm, and <0.075 mm were mixed. Then, the  
 151 mixture was tested on a BPG-907A experiment table for the temperature-programmed oxidation.  
 152 The heating rate was 0.3  $^{\circ}\text{C}/\text{min}$ , the temperature range was 30  $^{\circ}\text{C}$  to 170  $^{\circ}\text{C}$ , and the airflow rate  
 153 was 120 mL/min. With every 10  $^{\circ}\text{C}$  increase, the exit gas was drawn to analyse its composition  
 154 (especially  $\text{O}_2$ ,  $\text{CO}$ ,  $\text{CO}_2$ , and  $\text{C}_n\text{H}_m$ ) and concentration using a gas chromatograph. The test was  
 155 terminated when the temperature of the coal sample was higher than or equal to the temperature of  
 156 the furnace chamber (i.e. critical temperature).

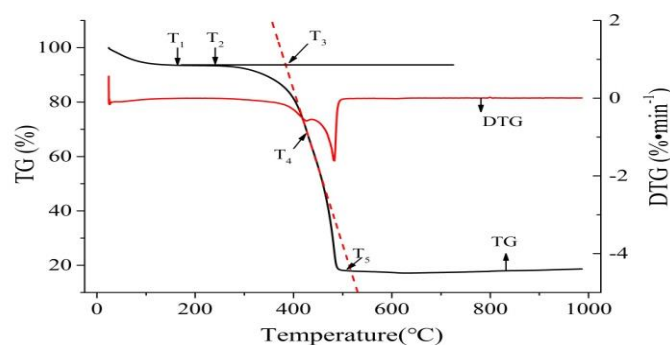
157 2.2.3 TGA Analysis

158 A STA 7300 thermal analyser (made by Hitachi, Japan) was used. The experimental  
 159 conditions were as follows: The heating rate was 10  $^{\circ}\text{C}/\text{min}$ , the atmosphere was air, the airflow  
 160 rate was 200 mL/min, and the temperature increased from the ambient temperature to 1000  $^{\circ}\text{C}$ .

161 2.3 Data Processing

162 2.3.1 Characteristic Temperatures

163 Thermogravimetric curves were generated using the TGA data (the particle size of coal  
 164 sample from SKS was 0.15-0.18 mm) (as shown in Fig. 2).



165

166

Fig. 2. TG and DTG curves of coal sample

167 As shown in Fig. 2,  $T_1$  to  $T_5$  denote the characteristic temperature of the coal at different  
 168 stages. Specifically,  $T_1$  denotes the inflection temperature at which a coal sample gains weight  
 169 after water loss and oxygen uptake;  $T_2$  denotes the initial temperature of pyrolysis;  $T_3$  denotes the  
 170 ignition temperature;  $T_4$  denotes the temperature at which the combustion rate is maximised, and  
 171  $T_5$  denotes the burn-off temperature.

### 172 2.3.2 Calculating the non-isothermal gasification kinetics parameters

173 The activation energy was calculated using the Coats-Redfern integral method. The  
 174 combustion reaction between coal and oxygen is viewed as a first-order reaction. According to the  
 175 Arrhenius, the reaction rate of coal combustion can be calculated:

$$k = A \exp\left(-\frac{E}{RT}\right) \quad (1)$$

177 where  $k$  denotes the reaction rate constant,  $A$  denotes the frequency factor,  $E$  denotes the activation  
 178 energy (kJ/mol),  $T$  denotes the reaction temperature (K), and  $R$  denotes the gas constant ( $R = 8.314$   
 179 J/(mol·K)).

180 In the coal-oxygen reaction process, the mass conversion rate is as follows:

$$\alpha = \frac{m_0 - m_t}{m_0 - m_\infty} \quad (2)$$

182 where  $\alpha$  denotes the mass conversion rate in the combustion process of coal sample,  $m_0$  denotes  
 183 the mass of the coal sample when the thermogravimetric experiment began,  $m_t$  denotes the mass of  
 184 coal sample  $t$  after the beginning of the experiment, and  $m_\infty$  denotes the mass of the coal sample at  
 185 the end. The reaction rate is calculated as follows:

$$\frac{d\alpha}{dt} = k(1 - \alpha) \quad (3)$$

187 where  $k$  denotes the chemical reaction rate, and  $t$  denotes time.

188 The following equations were obtained after the integral operation and the Coats-Redfern  
 189 approximate function were calculated:

$$n = 1, \ln\left[\frac{-\ln(1 - \alpha)}{T^2}\right] = \ln\left[\frac{AR}{\beta E}\left(1 - \frac{2RT}{E}\right)\right] - \frac{E}{RT} \quad (4)$$

$$n \neq 1, \ln\left[\frac{1 - (1 - \alpha)^{1-n}}{T^2(1 - n)}\right] = \ln\left[\frac{AR}{\beta E}\left(1 - \frac{2RT}{E}\right)\right] - \frac{E}{RT} \quad (5)$$

192 For the general reaction temperature province and activation energy ( $E$ ),  $E/RT$  is greater than  
 193 or equal to 1, and  $1 - 2RT/E$  is approximately 1. Therefore, Equation (4) can be rewritten as  
 194 Equation (6) when  $n$  is equal to 1.

$$\ln\left[\frac{-\ln(1 - \alpha)}{T^2}\right] = -\frac{E}{RT} \quad (6)$$

196 Equation (6) was used to calculate the kinetic parameters of the coal-oxygen reaction of the  
 197 samples. The vertical axis of  $\ln[-\ln(1-\alpha)/T^2]$  and horizontal axis of  $1/T$  were graphed, with the  
 198 slope of the linear fitting used to determine the activation energy.

### 199 3. Results and Discussion

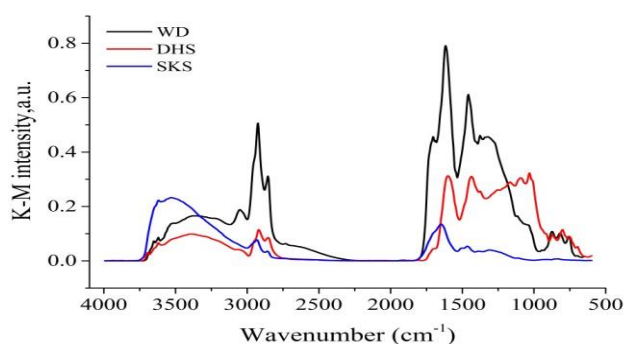
#### 200 3.1 Analysis of functional groups in coal molecules

201 Coal has a complex macromolecular structure that is mainly composed of aromatic  
 202 compounds with poor condensation, aliphatic hydrocarbons, oxygen-containing functional groups,  
 203 and other active groups. Infrared spectroscopy was used to study the basic chemical characteristics  
 204 of the coal samples. Table 2 lists the functional groups detected through the in-situ infrared  
 205 analysis of our coal samples.

206 Table 2

207 Characteristics of absorption peaks of the coal samples

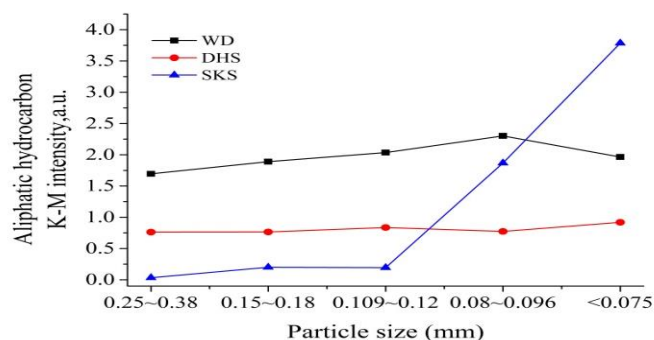
Spectral Peak No.	Spectral Peak Position	Functional Group	Classification
1	3624 – 3613	-OH	Intramolecular hydrogen bond
2	3500 – 3200	-OH	Intermolecular associated hydrogen bonds of phenolic hydroxyl, alcoholic hydroxyl or amidogen
3	2975 – 2915	-CH <sub>2</sub> , -CH <sub>3</sub>	Asymmetric stretching vibration of methyl and methylene
4	2875 – 2858	-CH <sub>2</sub> , -CH <sub>3</sub>	Symmetric stretching vibration of methyl and methylene
5	1625 – 1575	C=C	Deformation vibration of C=C in the aromatic nucleus
6	1470 – 1430	-CH <sub>2</sub> -CH <sub>3</sub>	Shear vibration of methylene
7	1379 – 1373	-CH <sub>3</sub>	Shear vibration of methyl
8	1350 – 1130	C-O	Bond of oxygen to phenol, alcohol, ether, and ester
9	900 – 700	-CH	Out-of-plane bending of substituted benzene C-H



209

Fig. 3. Infrared spectra with different coal samples

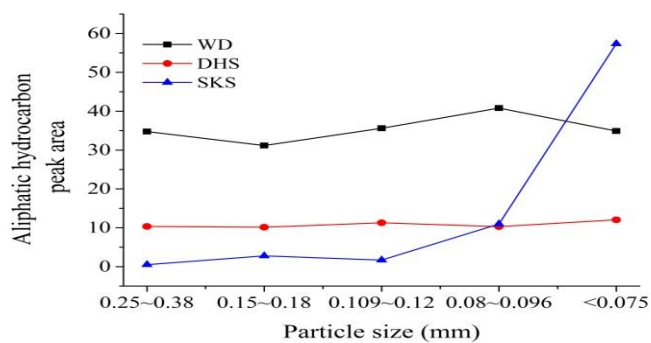
210 Fig. 3 shows the infrared spectra of coal samples from the three coal mines with a particle  
211 size of 0.15 to 0.18 mm. The spectra vary significantly, but indicate consistent primary functional  
212 groups. The coal samples from the WD and DHS mines share a consistent number of peaks, with  
213 fewer peaks for the coal sample from the SKS mine. In the wavenumber ranges of 3,624–3,613  
214  $\text{cm}^{-1}$  and 3,500–3,200  $\text{cm}^{-1}$ , the associated functional groups include the free hydroxyl group  
215 (-OH), intramolecular hydrogen bonds (-OH), and intermolecular hydrogen bonding (-OH) of a  
216 phenolic hydroxyl group, alcoholic hydroxyl group, or amidogen. The intensity of the infrared  
217 absorption peaks are ranked as follows: SKS > WD > DHS. In the wavenumber ranges of 2,975–  
218 2,915  $\text{cm}^{-1}$  and 2,875–2,858  $\text{cm}^{-1}$ , the associated functional groups include -CH<sub>2</sub> and -CH<sub>3</sub>, namely,  
219 the asymmetric stretching vibration of methyl and methylene. In terms of the intensity of infrared  
220 absorption peak, coal samples are ranked as follows: WD > DHS > SKS. In the wavenumber  
221 range of 1,625–1,575  $\text{cm}^{-1}$ , the associated functional group is C=C, with the deformation vibration  
222 of C=C in the aromatic nucleus. In terms of the intensity of infrared absorption peak, coal samples  
223 are ranked as follows: WD > DHS > SKS. From 1,449–1,439  $\text{cm}^{-1}$ , the associated functional group  
224 is -CH<sub>2</sub>-CH<sub>3</sub> as the shear vibration of methylene. From 1,379–1,373  $\text{cm}^{-1}$ , the associated  
225 functional group is -CH<sub>3</sub>, namely, shear vibration of methyl. In terms of the intensity of infrared  
226 absorption peak, coal samples are ranked as follows: WD > DHS > SKS. In the range of 1,350–  
227 1,130  $\text{cm}^{-1}$ , the associated functional group is C-O, as the bonding of oxygen to phenol, alcohol,  
228 ether, and ester. For 900–700  $\text{cm}^{-1}$ , the associated functional group is -CH, namely, the  
229 deformation vibration of diverse substituted aromatic hydrocarbons. In terms of the intensity of  
230 infrared absorption peak, coal samples are ranked as follows: DHS > WD > SKS.



231

232

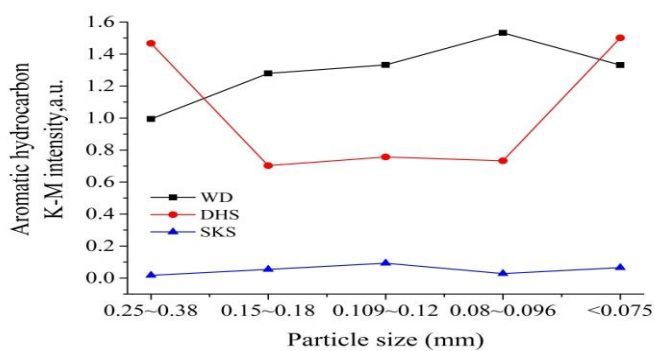
Fig. 4. Change in absorbance of aliphatic hydrocarbons with different particle sizes



233

234

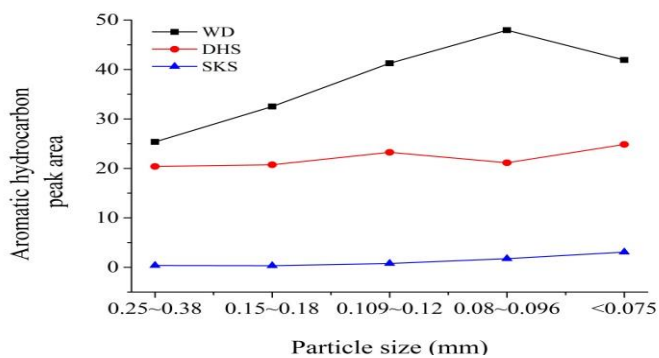
Fig. 5. Change in peak area of aliphatic hydrocarbons with different particle sizes



235

236

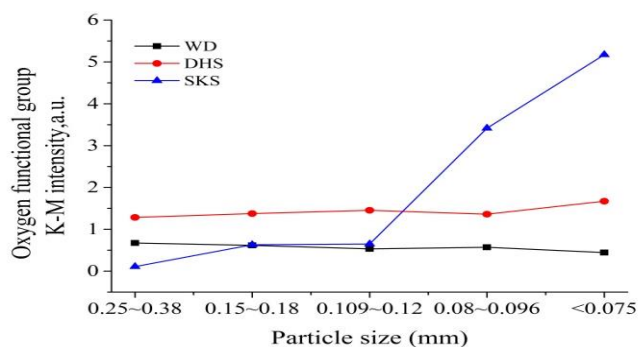
Fig. 6. Change in absorbance of aromatic hydrocarbons with different particle sizes



237

238

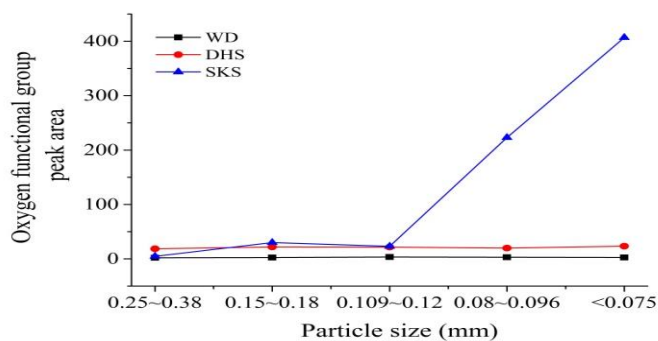
Fig. 7. Change in peak area of aromatic hydrocarbons with different particle sizes



239

240

Fig. 8. Change in absorbance of oxygen functional groups with different particle sizes



241

242 Fig. 9. Change in peak area of oxygen functional groups with different particle sizes

243 As shown in the figures above, the functional groups display consistent trends for the  
 244 absorbance and peak areas. As the particle size decreases, the absorbance and peak areas of  
 245 aliphatic hydrocarbons vary as follows: 1) for the coal samples from WD, the absorbance  
 246 increases first and then decreases; the peak areas decrease first, then increase before finally  
 247 decreasing again; 2) for the coal samples from DHS, the absorbance and peak areas do not vary  
 248 significantly; 3) for the coal samples from SKS, both the absorbance and peak areas increase (as  
 249 shown in Fig. 4 and Fig. 5). The absorbance and peak areas for the aliphatic hydrocarbons in the  
 250 coal samples are ranked as WD > DHS > SKS for particle size ranges of 0.25–0.38 mm, 0.15–0.18  
 251 mm, and 0.109–0.12 mm, WD > SKS > DHS for 0.08–0.096 mm, and DHS > WD > SKS for  
 252 those <0.075 mm.

253 As the particle size decreases, the absorbance and peak area of the aromatic hydrocarbons  
 254 vary as follows: 1) for the coal samples from WD, the absorbance and peak area increase first and  
 255 then decrease; 2) for those from DHS, the absorbance decreases first and then increases, and the  
 256 peak area increases first, then decreases, and finally increases; 3) for the samples from SKS, the  
 257 absorbance increases first, then decreases, and finally increases, and the peak area increases (as  
 258 shown in Fig. 6 and Fig. 7). The absorbance of the aromatic hydrocarbons in coal samples are  
 259 ranked as follows: DHS > WD > SKS for particle size ranges of 0.25–0.38 mm and <0.075 mm,  
 260 WD > DHS > SKS for 0.15–0.18 mm, 0.109–0.12 mm, and 0.08–0.096 mm; WD > DHS > SKS  
 261 for all particle size ranges overall.

262 As the particle size decreases, the absorbance and peak area of oxygen-containing functional  
 263 group vary as follows: 1) for the samples from WD, the absorbance decreases, whereas for those  
 264 from DHS and SKS, the absorbance increases; 2) for the samples from WD and DHS, the peak  
 265 area does not vary significantly, whereas for those from SKS, the peak area increases first, then

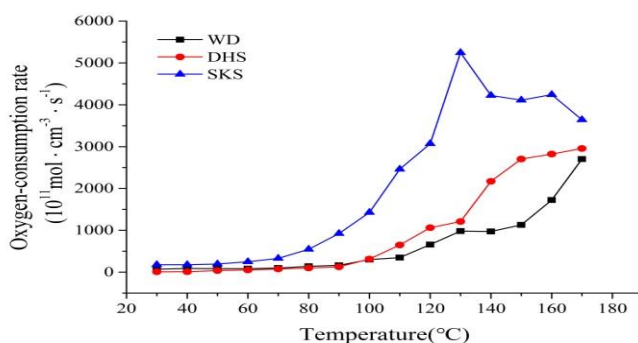
266 decreases, and finally increases (as shown in Fig. 8 and Fig. 9). The absorbance of the  
267 oxygen-containing functional group in the coal samples are ranked as follows: DHS > WD > SKS  
268 for the particle size range of 0.25–0.38 mm, DHS > WD > SKS for 0.15–0.18 mm, DHS > SKS >  
269 WD for 0.109–0.12 mm, and SKS > DHS > WD for 0.08–0.096 mm and <0.075 mm.

270 As mentioned in previous studies, the content of oxygen-containing functional groups is an  
271 index to measure if the coal is prone to oxidation. The experimental data reveal that for coal  
272 samples from SKS, the smaller the particle size is, the more prone the coal samples are to  
273 oxidation, and the particle size does not affect the oxidation propensity of the samples from WD  
274 and DHS. Elemental analysis of the coal samples determined that the proportions of oxygen  
275 elements are ranked as WD > SKS > DHS. In summary, coal samples from SKS are the most  
276 prone to oxidation, followed by WD, then DHS.

## 277 3.2 Analysis of coal oxidation properties

### 278 3.2.1 Analysis of temperature-programmed oxidation

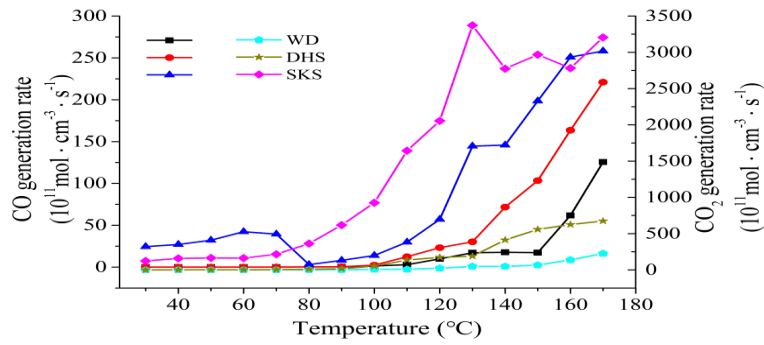
279 In the temperature-programmed adiabatic oxidation experiment, we mainly tested how the  
280 concentrations of O<sub>2</sub>, CO<sub>n</sub> and C<sub>n</sub>H<sub>m</sub> gas varied with the rise in the reaction temperature of the  
281 coal samples at the low-temperature oxidation stage. We used this data to establish the relative  
282 difficulty of spontaneous combustion for the coal samples. Using the characteristic parameters, we  
283 predicted and determined the degree of spontaneous combustion oxidation of the coal in the  
284 sections studied, as well as the degree of environmental pollution.



285

286

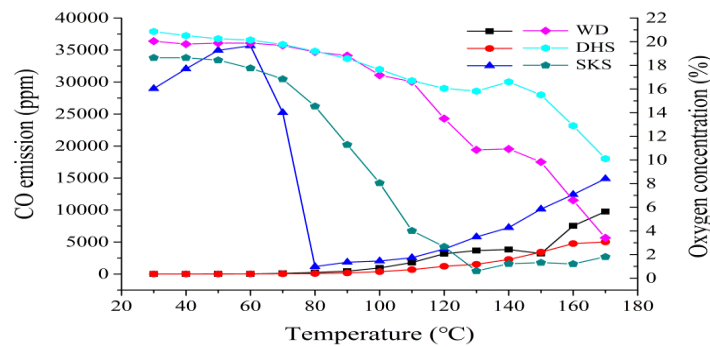
Fig. 10. Oxygen consumption rate



287

288

Fig. 11. Generation rate of CO and CO<sub>2</sub>



289

290

Fig. 12. CO emission concentration and oxygen concentration

291

Oxygen consumption rate is an index to measure the intensity of the coal-oxygen reaction.

292

For the samples from WD and DHS, the oxygen consumption rate positively correlated with

293

temperature, and for those from SKS, the oxygen consumption rate increased first and then

294

decreased with the rise in temperature (as shown in Fig. 10).

295

As shown in Fig. 11, the coal samples are ranked as follows by the yield of CO and CO<sub>2</sub>:

296

SKS > DHS > WD. In addition to the CO<sub>2</sub> generation rate of SKS coal sample higher than the CO

297

generation rate, the CO<sub>2</sub> output rate of the other two mines are lower than the CO generation rate.

298

This indicates that coal combustion in SKS produces the most severe environmental pollution,

299

followed by DHS, and then WD.

300

The emission concentration of CO is positively correlated with temperature for the samples

301

from WD and DHS, and for those from SKS, the emission concentration is high initially, then

302

follows the same trend as that of the samples from WD and DHS after temperature reaches 80 °C

303

(as shown in Fig. 12). For the coal samples from WD and DHS, the emission concentration of CO

304

increases slowly when the temperature is below 90 °C, then displays a marked increase over 90 °C,

305

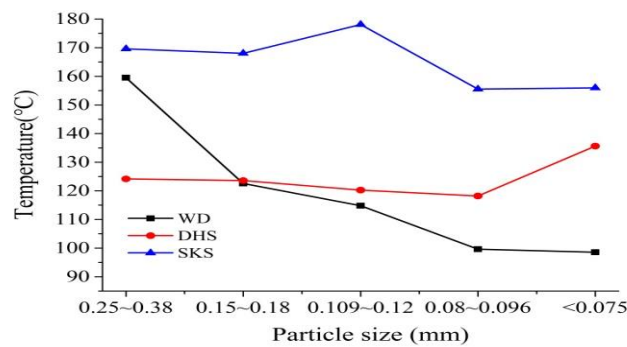
indicating a speed-up in the oxidation reaction. After temperature is above 130 °C, the emission

306

concentration of CO increases sharply, indicating a further speed-up in the oxidation reaction. For

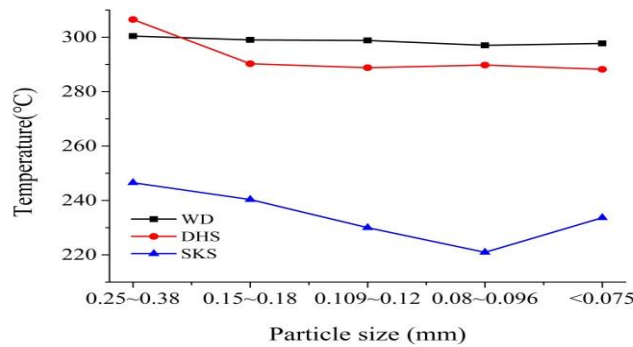
307 the coal samples from SKS, the emission concentration of CO is quite high initially, indicating that  
 308 the oxidation reaction is quite fast initially, and then slows down until the degree of oxidation is  
 309 the same as that of the samples from WD and SKS. For the samples from the three coal mines, the  
 310 concentration of oxygen basically shares the same trend with the rise in temperature (decrease first,  
 311 and then increase when temperature reaches 130 °C). The concentration of oxygen increases first  
 312 with a sharp decrease for the samples from WD and DHS; for SKS, the concentration of oxygen  
 313 continues to increase, but at a lower rate than that of the samples from WD and DHS.

314 3.2.2 Characteristic temperature of coal by TG and DTG analyses



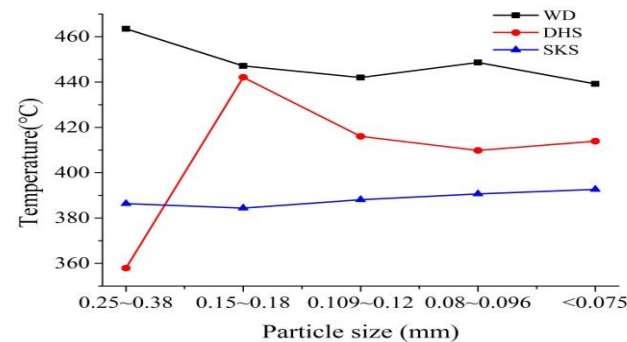
315

316 Fig. 13. T<sub>1</sub> of characteristic temperatures of coal samples with different particle sizes



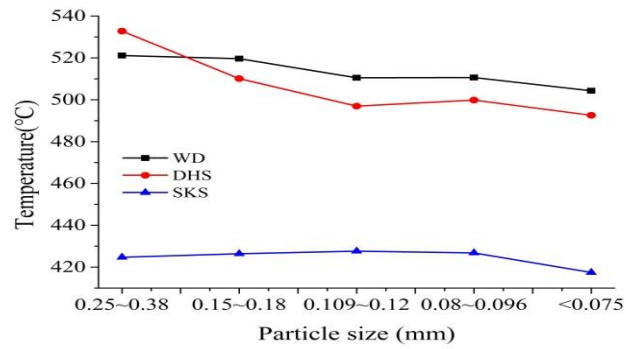
317

318 Fig. 14. T<sub>2</sub> of characteristic temperatures of coal samples with different particle sizes



319

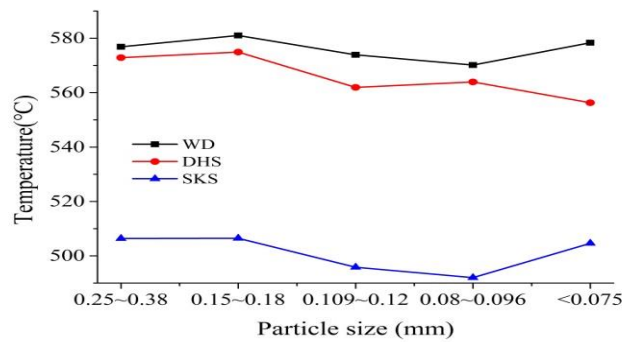
320 Fig. 15. T<sub>3</sub> of characteristic temperatures of coal samples with different particle sizes



321

322

Fig. 16. T<sub>4</sub> of characteristic temperatures of coal samples with different particle sizes



323

324

Fig. 17. T<sub>5</sub> of characteristic temperatures of coal samples with different particle sizes

325

326

327

328

329

As shown in Figures 13 – 17, the characteristic temperatures T<sub>2</sub>, T<sub>3</sub>, T<sub>4</sub>, and T<sub>5</sub> of the coal samples from SKS are all lower than those from WD and DHS, whereas the characteristic temperature T<sub>1</sub> of the samples from SKS is higher than that from WD and DHS. As the particle size decreased, the T<sub>1</sub> decreased for the samples from WD, decreased first and then increased for DHS samples, and increased first and then decreased for SKS samples.

330

331

332

333

334

335

336

As the particle size decreases, the T<sub>2</sub> for the WD samples varies slightly, decreases first and then varies slightly for DHS, and decreases first and then increases for SKS. As the particle size decreases, the T<sub>3</sub> for the WD samples decreases first, then increases, and finally decreases. The T<sub>3</sub> of the samples from DHS increases first, then decreases, and finally increases, and the T<sub>3</sub> for SKS decreases first and then increases. Because T<sub>3</sub> denotes the ignition temperature of coal, the lower the ignition temperature is, the more prone the coal is to spontaneous combustion. Therefore, the coal from SKS is the most prone to spontaneous combustion, followed by DHS, and then WD.

337

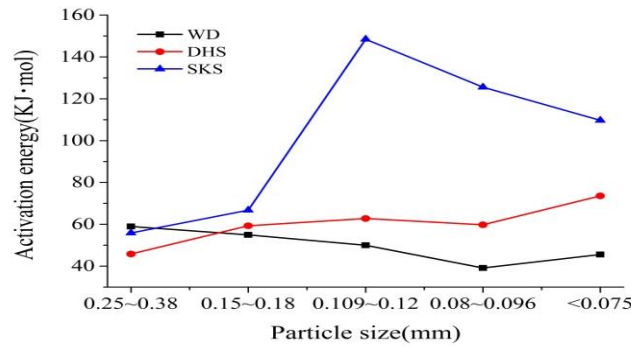
338

339

340

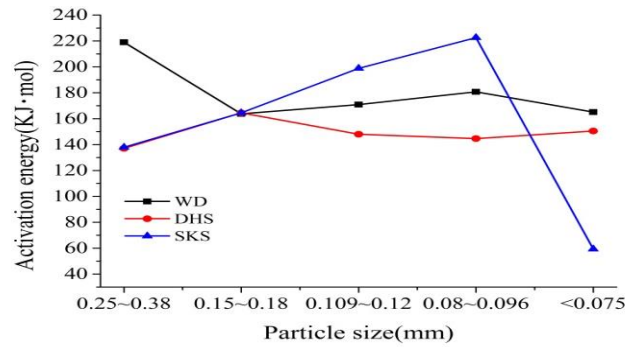
As the particle size decreases, the T<sub>4</sub> of the samples from WD and DHS tend to decrease, and the T<sub>4</sub> of those from SKS increases first and then decreases. For the T<sub>5</sub>, the samples from WD show an increase first, then a decrease, and finally an increase. The T<sub>5</sub> of the coal samples from DHS varies irregularly, and the T<sub>5</sub> of the SKS samples decreased before increasing.

341 3.2.3 Analysis of Activation Energy



342

343 Fig. 18. Activation energy of coal sample at the T<sub>1</sub>-T<sub>2</sub> stage with different particle sizes



344

345 Fig. 19. Activation energy of coal sample at the T<sub>3</sub>-T<sub>5</sub> stage with different particle sizes

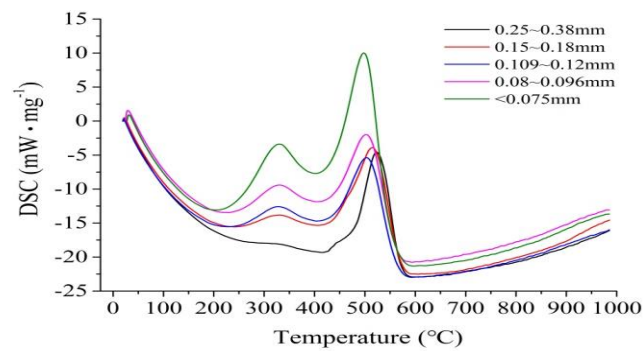
346 As shown in Fig. 18 and Fig. 19, during the low-temperature oxidation stage, the activation  
 347 energy of the samples from DHS and SKS increases first and then decreases overall, from WD,  
 348 decreases first and then increases, and from DHS, is higher than that from WD and SKS. During  
 349 the high-temperature oxidation combustion stage, the activation energy for the DHS and SKS  
 350 samples increases first and then decreases, and the activation energy for WD decreases first and  
 351 then increases. Based on the proximate analysis, the coal samples are ranked as follows by volatile  
 352 components: SKS > DHS > WD. For the SKS samples, the volatile content is the highest, and the  
 353 T<sub>3</sub> and T<sub>5</sub> are lower than those for WD and DHS. Therefore, a higher volatile content indicates that  
 354 the samples are more prone to ignition, and the coal samples burned out more readily.

355 Volatile content is not the only factor that affects the characteristic temperatures (e.g. element  
 356 content), nor does it only impact the characteristic temperatures. The activation energy of the coal  
 357 tends to decline with higher volatile components, so the coal particles will be more likely to ignite.  
 358 In addition, the precipitation of volatiles changes the morphological structure of the coke, making  
 359 the residual coke porous, resulting in a larger specific surface area and air contact area, thus  
 360 making the residual coke more prone to oxidation and combustion. As a result, the minimum

361 energy required for coal combustion (i.e. activation energy) is lower (Table 1).

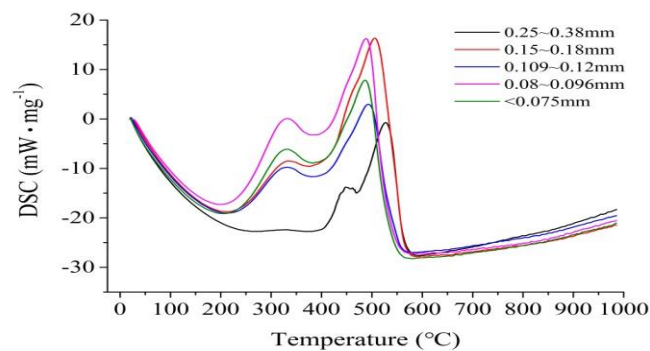
### 362 3.2.4 Analysis of exothermic heat in the oxidation process of coal

363 DSC was performed to measure the quantity of heat required for maintaining a  
364 zero-temperature difference per unit time between a sample and a reference object to reflect how  
365 the enthalpy of the sample varies with temperature. DSC curves were generated from the  
366 thermogravimetric data using the Origin software. Specifically, the integral operation was  
367 conducted on the X axis to determine the exothermic heat at different stages of spontaneous  
368 combustion. In the graph, below 0 on the Y axis is the heat absorbed by spontaneous combustion,  
369 and above 0 of the Y axis is the exothermic heat of spontaneous combustion. According to the  
370 characteristic temperatures determined by the thermogravimetric experiment, the coal-oxygen  
371 reaction process is divided into three stages: 1) oxygen absorption and weight-gaining stage  
372 ( $T_1$ - $T_2$ ), 2) dehydration stage ( $T_2$ - $T_3$ ), and 3) combustion stage ( $T_3$ - $T_5$ ). In this study, only the  
373 exothermic heat at the combustion stage was calculated. Figures 12 to 14 respectively show the  
374 DSC curves of coal samples from WD, DHS, and SKS. Figure 15 shows the exothermic heat of  
375 the coal samples with different particle sizes from the three mines at the combustion stage.



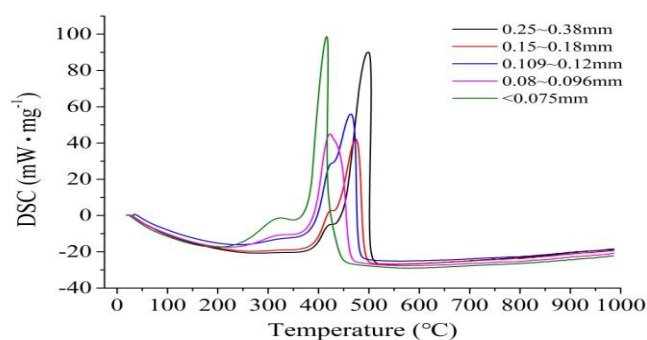
376

377 Fig. 20. DSC curves of coal samples from the WD mine with different particle sizes



378

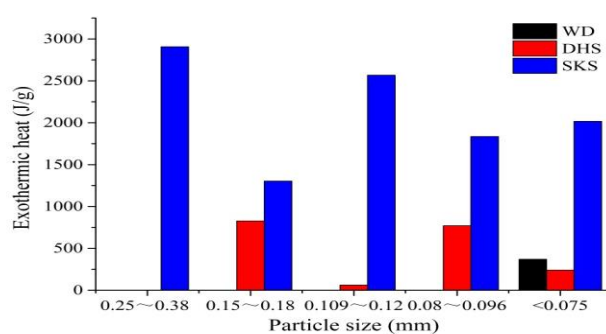
379 Fig. 21. DSC curves of coal samples from the DHS mine with different particle sizes



380

381

Fig. 22. DSC curves of coal samples of the SKS mine with different particle sizes



382

383

Fig. 23. Exothermic heat of the coal samples with different particle sizes

384

385

386

387

388

389

390

391

392

393

394

395

396

397

398

399

As shown in Fig. 20 to 22, the DSC curves of the samples from the three coal mines reflect their exothermic heat. Among the samples from WD, exothermic heat was only recorded for particle sizes of <0.075 for oxidation reactions, indicating low exothermic heat generated by oxidation reactions. Among the coal samples from DHS, the DSC values for particle sizes of 0.15–0.18 mm, 0.08–0.096 mm, and <0.075 mm are greater than 0 (i.e. exothermic heat is generated), indicating average exothermic heat generated by oxidation reactions. For both WD and DHS, smaller particle sizes are beneficial to the generation of exothermic heat. For the SKS samples, all particle sizes record exothermic heat, indicating high exothermic heat generated by oxidation reactions. Additionally, the samples with a particle size of <0.075 mm are different from those with a particle size of 0.25–0.38 mm in terms of peak height and peak width. As shown in the above figures, however, both particle sizes generate high exothermic heat during the oxidation reaction.

Fig. 23 demonstrates that the coal samples from WD generate the lowest exothermic heat, followed by DHS and SKS. Additionally, the exothermic heat generated by the SKS samples with different particle sizes varies irregularly but is overall higher than that from WD and DHS. Therefore, the coal samples from SKS are the most prone to spontaneous combustion.

#### 400 **4. Conclusions**

401 First, elemental analysis shows that, overall, the content of oxygen-containing functional  
402 groups tends to increase with the decrease in particle size; therefore, the smaller the particle size is,  
403 the more prone the coal samples are to oxidation and spontaneous combustion. The proportions of  
404 oxygen in the samples is ranked as  $WD > SKS > DHS$ . In summary, the coal samples from SKS  
405 are the most prone to oxidation, followed by the WD samples, and the samples from DHS are least  
406 prone to oxidation.

407 Second, for coal samples from DHS and WD, the oxygen consumption rate continues to  
408 increase exponentially with the rise in temperature; for coal samples from SKS, oxygen  
409 consumption rate increases exponentially initially, and then decreases. The different gases  
410 emission show that the oxidation reaction speeds up at the temperatures of 90 °C and 130 °C.  
411 These gases show that coal samples from SKS are more prone to spontaneous combustion than  
412 those from DHS and WD. Furthermore, during this reaction, the samples from SKS produce more  
413 pollutants than those from DHS and WD.

414 Third, for coal samples from WD and DHS, the  $T_3$  declines as the particle size decreases,  
415 indicating that the smaller the particle size is, the lower the ignition temperature of coal sample is.  
416 For the SKS samples, the  $T_3$  rises as the particle size decreases, but the  $T_3$  of all sample particle  
417 sizes is lower than that of the samples from WD and DHS, indicating that coal samples from SKS  
418 are more prone to combustion.

419 The reaction activation energy of experimental coal samples overall tends to increase at the  
420 stage of low-temperature oxidation. At the stage of high-temperature oxidation, as the particle size  
421 decreases, the activation energy of the samples from WD and SKS decreases, whereas that of the  
422 DHS samples increases first and then decreases. Overall, at the stage of high-temperature  
423 oxidation combustion, lower activation energy implies that coal is more prone to ignition, causing  
424 a higher risk of spontaneous combustion.

425 Volatile content is also a factor that affects the spontaneous combustibility of the coal  
426 samples. Higher volatile contents cause the samples to be more prone to ignition and burn out  
427 sooner. The amount of exothermic heat reveals that in the SKS samples, higher exothermic heat  
428 indicates that the samples will be more prone to spontaneous combustion.

429 In practice, the fire areas in SKS generated by coal mining are still on fire, but not yet  
430 harnessed. This also indicates that coal of SKS is very prone to spontaneous combustion.

431 **Acknowledgements**

432 This work was supported by the Key Research & Development Program of Ministry of  
433 Science and Technology of China (grant No.2018YFC0807901-2); the National Natural Science  
434 Foundation of China (grant No. 51974275).

435 **References:**

- 436 Chuan Zh., Hua T., Yang B., 2019, Evaluation of slagging and fouling characteristics during  
437 Zhundong coal co-firing with a Si/Al dominated low rank coal [J], *Fuel*, 254.
- 438 Casal M. D., Vega M. F., Diaz-Faes E., 2018, The influence of chemical structure on the kinetics of  
439 coal pyrolysis[J], *International Journal of Coal Geology*, 195.
- 440 Cheng W., Hu X., Xie J., 2017, An intelligent gel designed to control the spontaneous  
441 combustion of coal: fire prevention and extinguishing properties[J], *Fuel*, 210:826–35.
- 442 Deng J., Zhang Y. X., Zhao J. Y., 2019, Experiment study on oxidation and activated energy of  
443 different partial size coal based on programmed temperature rising[J], *Coal Science and  
444 Technology*, 47(01):214-219.
- 445 Kong B., Li Z. H., Wang E. Y., 2018, An experimental study for characterization the process of  
446 coal oxidation and spontaneous combustion by electromagnetic radiation technique[J].  
447 *Process Safety and Environmental Protection*, 119:285-94.
- 448 Kong B., Li Z. H., Yang Y. L., 2017, A review on the mechanism, risk evaluation, and prevention  
449 of coal spontaneous combustion in China [J], *Environmental science and pollution research  
450 international*, 24(30) :23453-23470.
- 451 Liu W., Wang J., Bhattacharyya D., 2018, Economic and environmental analyses of coal and  
452 biomass to liquid fuels[J], *Energy*, 141: 76-86.
- 453 Lei C., Deng J., Cao K., 2018, A random forest approach for predicting coal spontaneous  
454 combustion[J], *Fuel*, 223:63-73.
- 455 Mustafa B., Alp Y., Burçin Y., 2016, Structure of some western Anatolia coals investigated by  
456 FTIR, Raman, <sup>13</sup>C solid state NMR spectroscopy and X-ray diffraction[J], *International  
457 Journal of Coal Geology*, 163.
- 458 Niu Q., Cao L., Sang S., 2017, The adsorption-swelling and permeability characteristics of natural  
459 and reconstituted anthracite coals[J], *Energy*, 141:2206-17.
- 460 Onifade M., Genc B., 2020, A review of research on spontaneous combustion of coal [J].  
461 *International Journal of Mining Science and Technology*, (prepublish).
- 462 Onifade M, Genc B., 2019, A review of spontaneous combustion studies-South African context [J].  
463 *International Journal of Mining, Reclamation and Environment*, 33(8):527-47.
- 464 Pan R. K., Li C., Yu M. G., 2020, Evolution patterns of coal micro-structure in environments with  
465 different temperatures and oxygen conditions[J], *Fuel*, 261.
- 466 Peña B., Pallarés J., Bartolomé C., Hecce C., 2018, Experimental study on the effects of co-firing  
467 coal mine waste residues with coal in PF swirl burners[J], *Energy*, 157.
- 468 Qu L. N., Song D. Z., Tan B., 2018, Research on the critical temperature and stage characteristics  
469 for the spontaneous combustion of different metamorphic degrees of coal[J], *International  
470 Journal of Coal Preparation and Utilization*, 38(5): 221-236.
- 471 Wang C., Yang S., Li J., 2018, Influence of coal moisture on initial gas desorption and gas-release  
472 energy characteristics[J], *Fuel*, 232:351-61.
- 473 Wang C. P., Xiao Y., Li Q. W., 2018, Free radicals, apparent activation energy, and functional  
474 groups during low-temperature oxidation of Jurassic coal in Northern Shaanxi[J],  
475 *International Journal of Mining Science and Technology*, 28(03) :469+474-475+470-473.
- 476 Xu Q., Yang S. Q., Cai J. W., 2018, Risk forecasting for spontaneous combustion of coals at  
477 different ranks due to free radicals and functional groups reaction[J], *Process Safety and*

478 Environmental Protection, 326-371.

479 Xiao Y. , Ren S. J., Deng J., 2018, Comparative analysis of thermokinetic behavior and gaseous  
480 products between first and second coal spontaneous combustion[J], Fuel, 227:325-333.

481 Yan D. W., Gu M. Y., Lin Y. Y., 2018, Evolution of surface functional groups of coal char during  
482 coal combustion under O<sub>2</sub>/CO<sub>2</sub> atmospheres[J], Asia-Pacific Journal of Chemical  
483 Engineering, 13(2).

484 Yang Sh., Dai G. L., Tang M. Y., 2018, Experiment Study on Mark Gas of Coal Spontaneous  
485 Combustion Based on Programmed Temperature Program[J], Safety in Coal Mines,  
486 49(07):24-27+33.

487 Zhang Y. T., Zhang Y. B., Li Y. Q., 2020, Study on the Characteristics of Coal Spontaneous  
488 Combustion during the Development and Decaying Processes [J]. Process Safety and  
489 Environmental Protection, (prepublish).

490 Zhang Y. T., Yang C. P., Li Y. Q., 2019, Ultrasonic extraction and oxidation characteristics of  
491 functional groups during coal spontaneous combustion[J], Fuel, 242: 287-294.

492 Zhao J. Y., Deng J., Chen L.,2019(a), Correlation analysis of the functional groups and exothermic  
493 characteristics of bituminous coal molecules during high-temperature oxidation[J], Energy  
494 181 : 136-147.

495 Zhao J. Y., Deng J., Wang T., 2019(b), Assessing the effectiveness of a  
496 high-temperature-programmed experimental system for simulating the spontaneous  
497 combustion properties of bituminous coal through thermokinetic analysis of four oxidation  
498 stages[J], Energy, 169 :587-596.

499 Zeng Q., Li G. Sh., Jin Sh. K., 2017, Characteristics of oxidation and spontaneous combustion of  
500 the major mining coal seam in Dajing area of Easter Junggar coalfield[J], China Mining  
501 Magazing, 26(01):98-103.

502 Zhang Y. N., 2004, Application of the Thermogravimetric Analysis in the Research of the  
503 Oxidation of Coal [D]. Xi'an University of Science and Technology.

# Figures

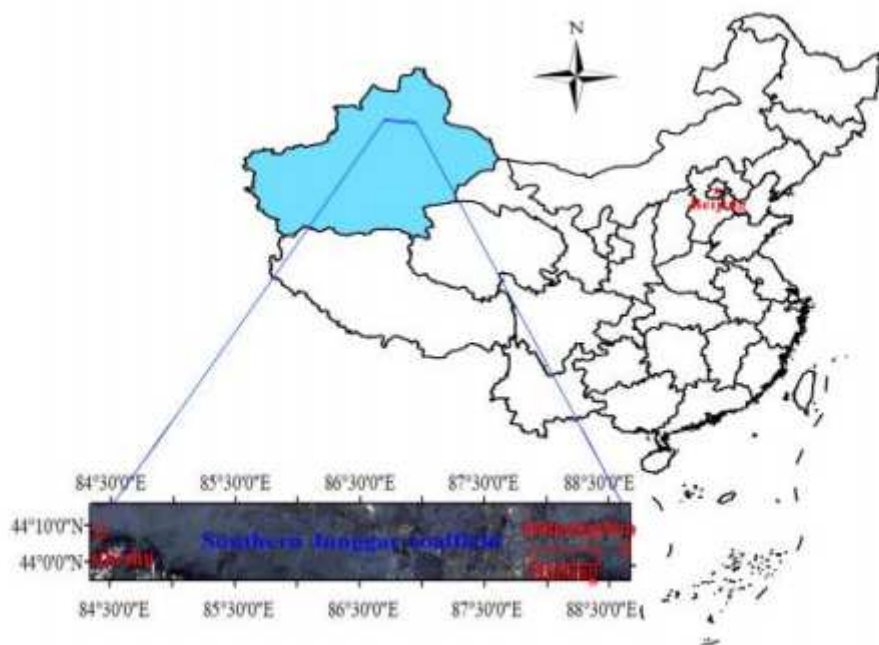


**Figure 1**

Location of study area. Note: The designations employed and the presentation of the material on this map do not imply the expression of any opinion whatsoever on the part of Research Square concerning the legal status of any country, territory, city or area or of its authorities, or concerning the delimitation of its frontiers or boundaries. This map has been provided by the authors.

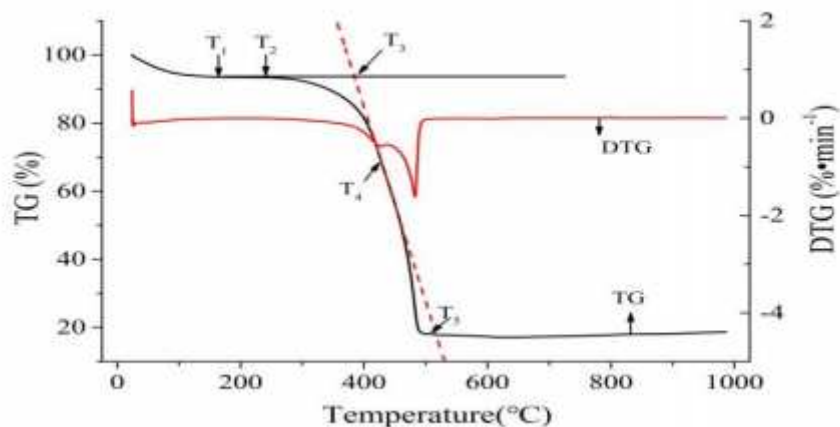


**Figure 2**

TG and DTG curves of coal sample

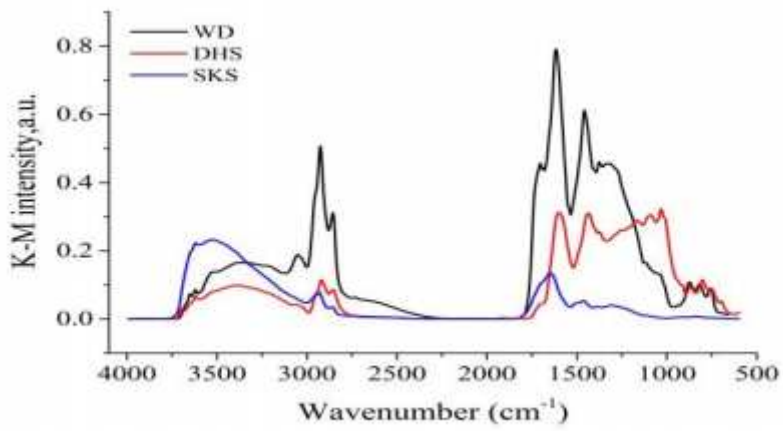


Figure 3

Infrared spectra with different coal samples

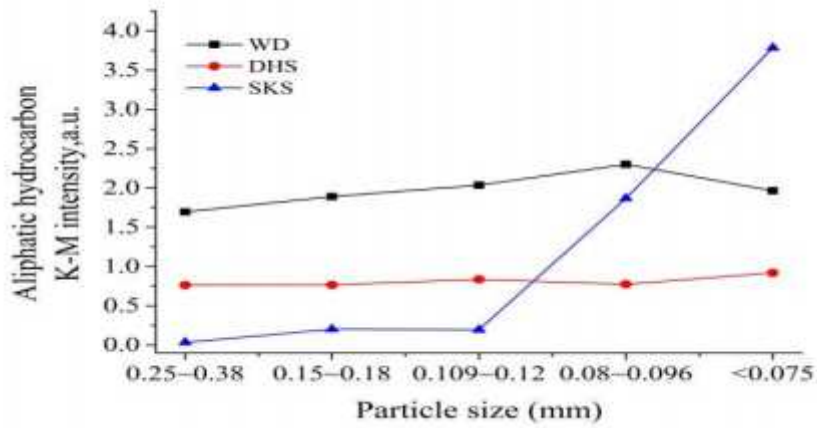
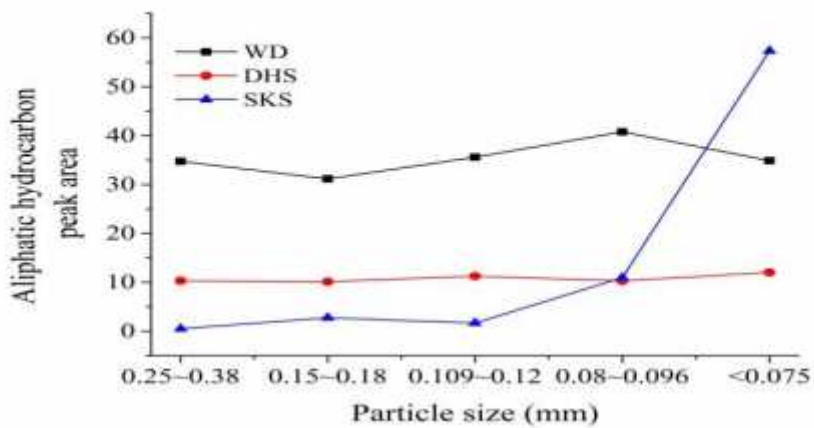


Figure 4

Change in absorbance of aliphatic hydrocarbons with different particle sizes



**Figure 5**

Change in peak area of aliphatic hydrocarbons with different particle sizes

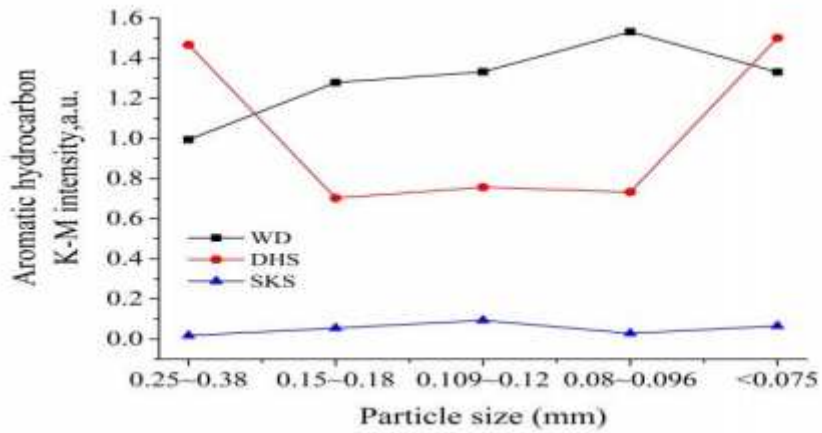


**Figure 6**

Change in absorbance of aromatic hydrocarbons with different particle sizes

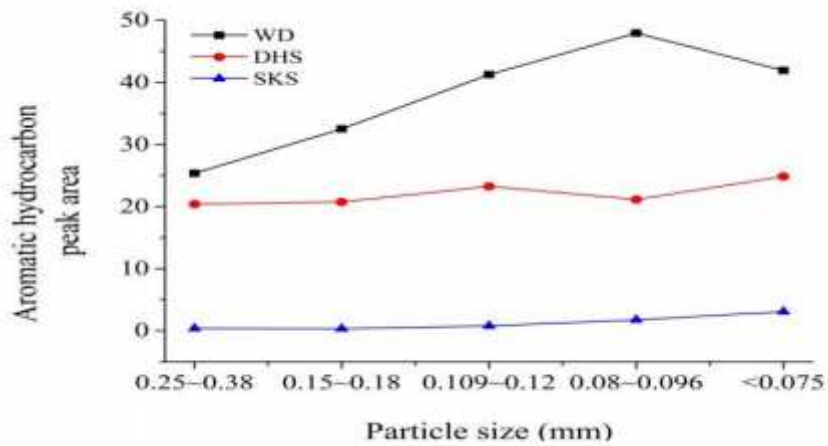


**Figure 7**

Change in peak area of aromatic hydrocarbons with different particle sizes

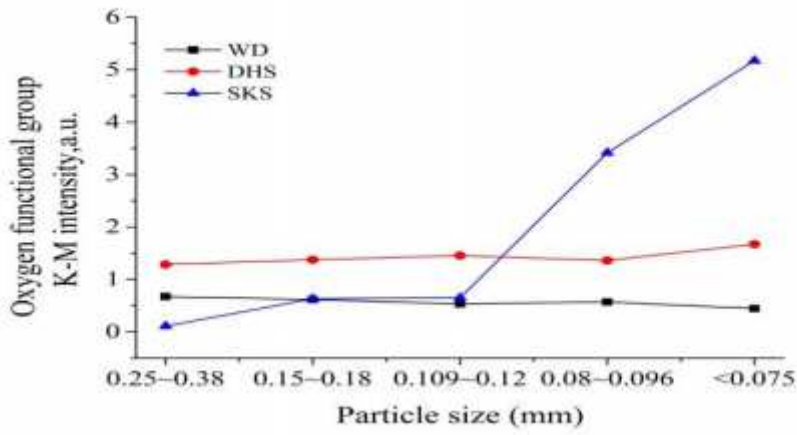


**Figure 8**

Change in absorbance of oxygen functional groups with different particle sizes

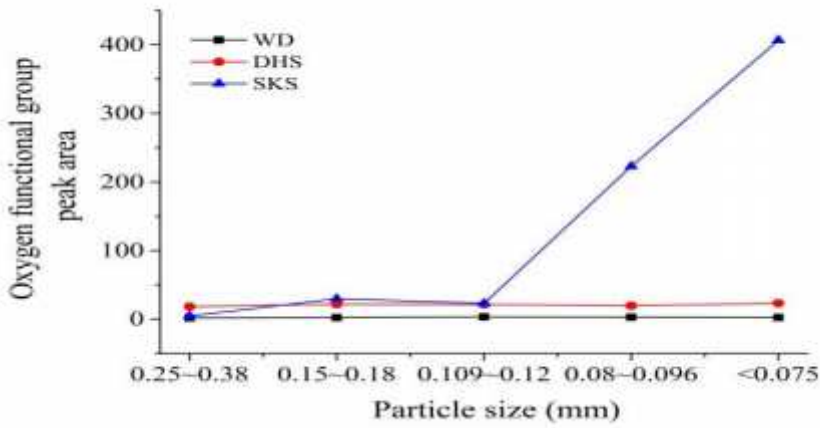


**Figure 9**

Change in peak area of oxygen functional groups with different particle sizes

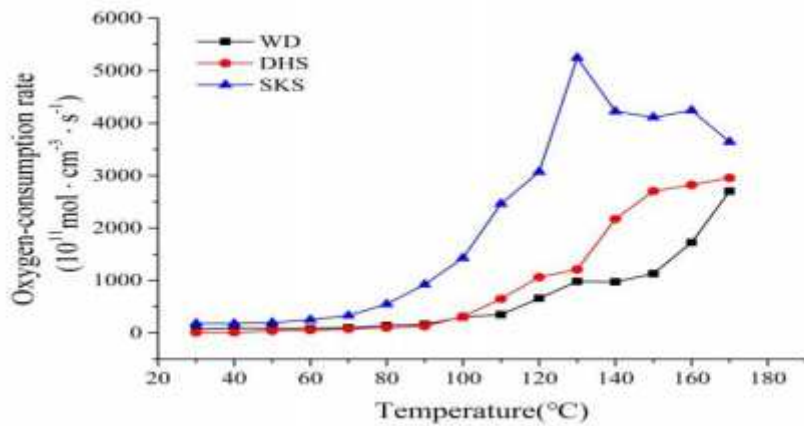


Figure 10

Oxygen consumption rate

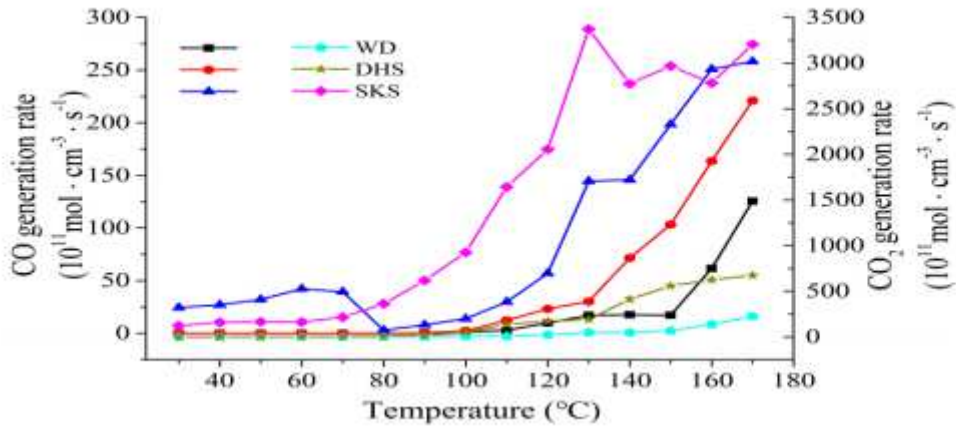


Figure 11

Generation rate of CO and CO<sub>2</sub>

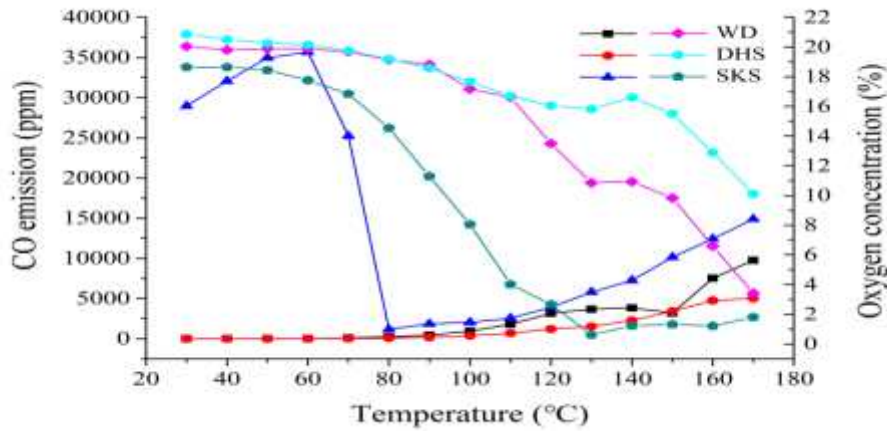


Figure 12

CO emission concentration and oxygen concentration

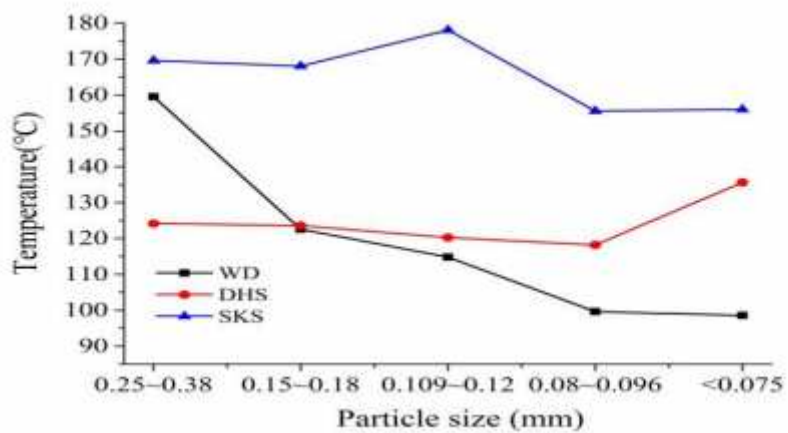


Figure 13

T1 of characteristic temperatures of coal samples with different particle sizes

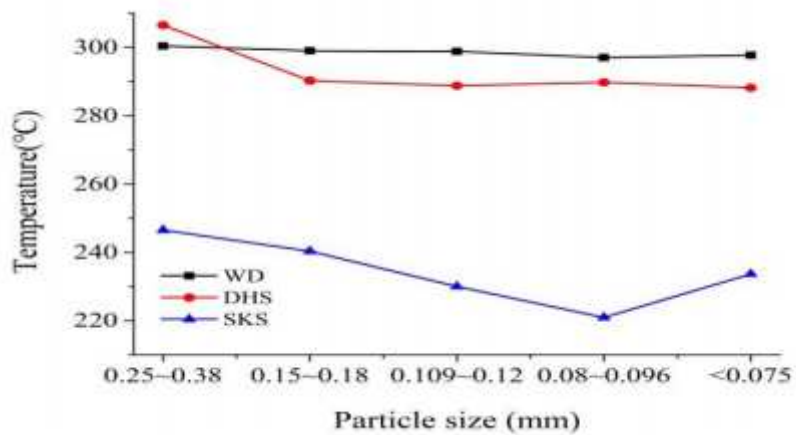


Figure 14

T2 of characteristic temperatures of coal samples with different particle sizes

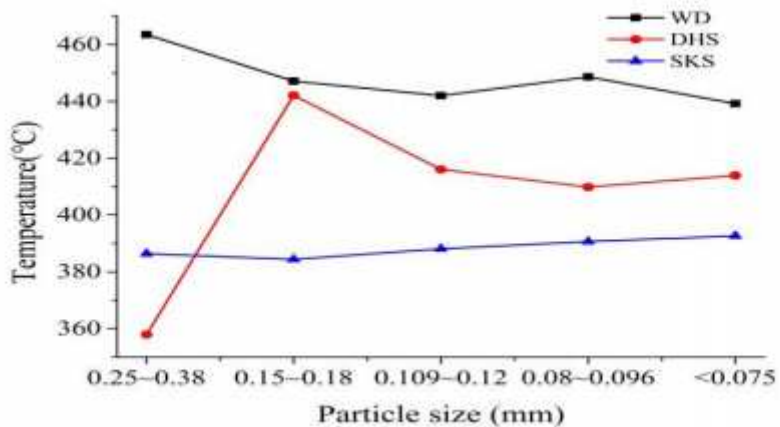


Figure 15

T3 of characteristic temperatures of coal samples with different particle sizes

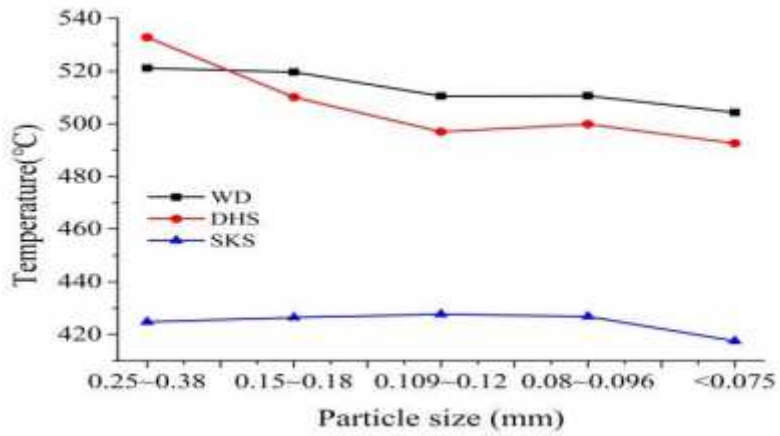


Figure 16

T4 of characteristic temperatures of coal samples with different particle sizes

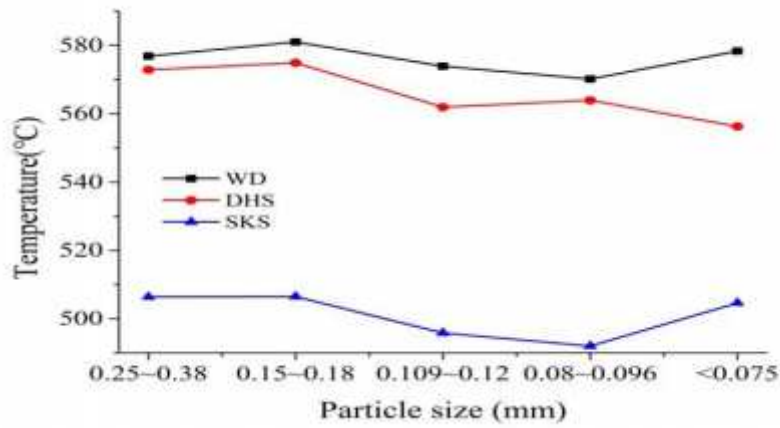
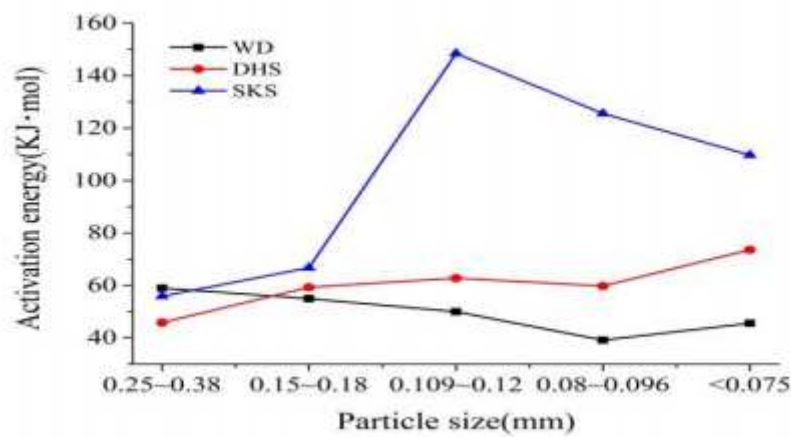


Figure 17

T5 of characteristic temperatures of coal samples with different particle sizes



**Figure 18**

Activation energy of coal sample at the T1-T2 stage with different particle sizes

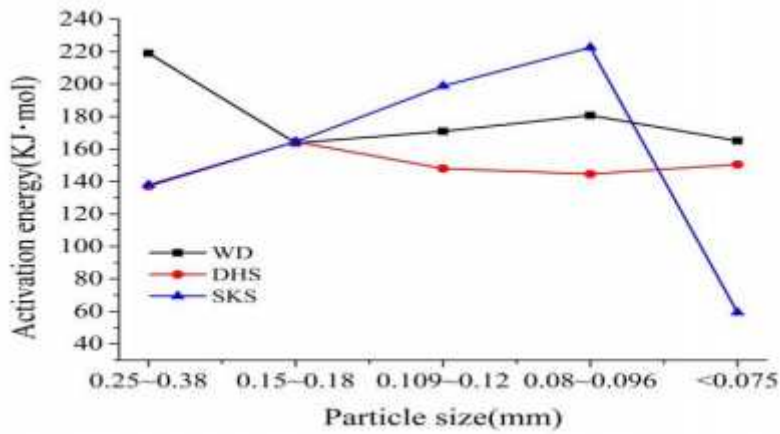


**Figure 19**

Activation energy of coal sample at the T3-T5 stage with different particle sizes

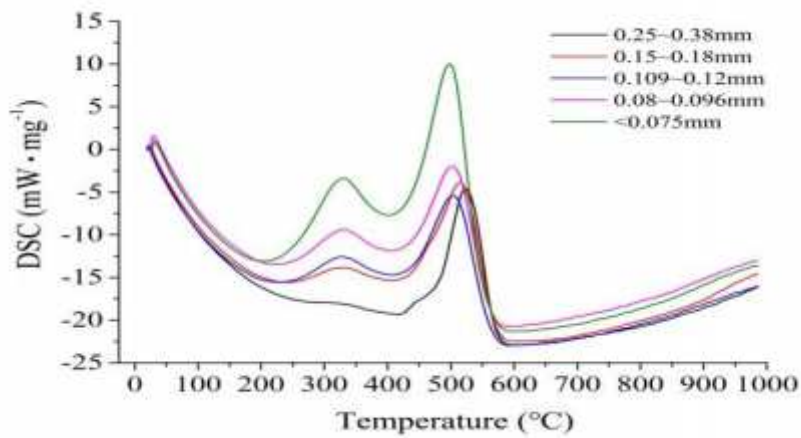


**Figure 20**

DSC curves of coal samples from the WD mine with different particle sizes

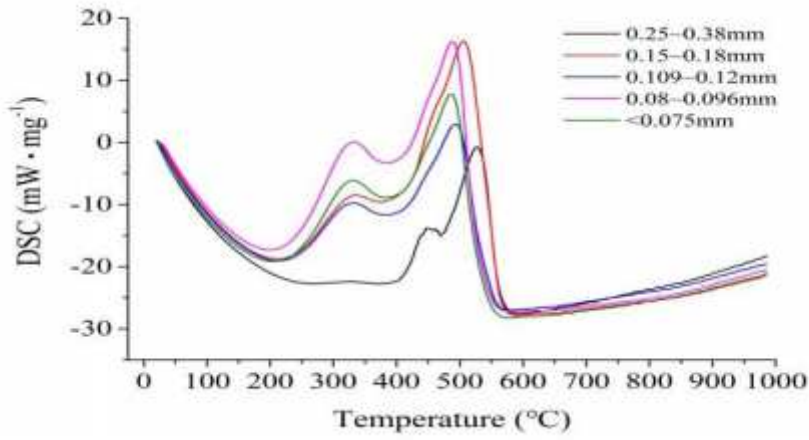


Figure 21

DSC curves of coal samples from the DHS mine with different particle sizes

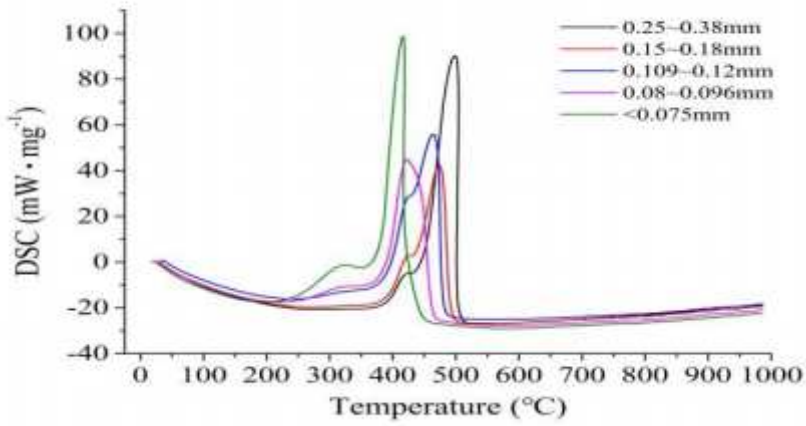


Figure 22

DSC curves of coal samples of the SKS mine with different particle sizes

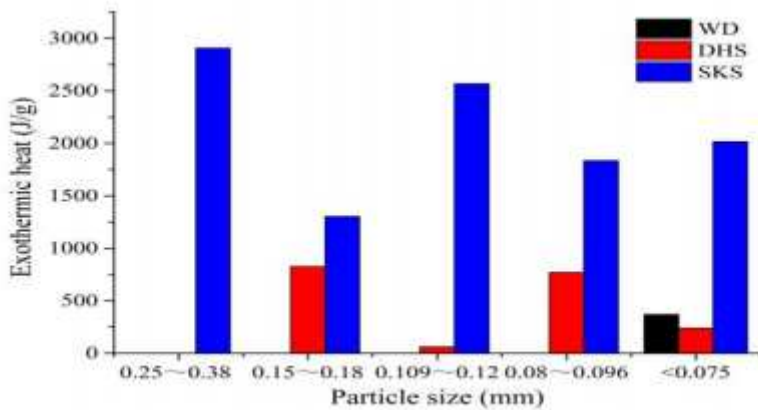


Figure 23

Exothermic heat of the coal samples with different particle sizes